

## Equilibrium Shapes and Their Stability for Liquid Films in Fast Flows

Likhit Ganedi,<sup>1</sup> Anand U. Oza,<sup>1,\*</sup> Michael Shelley,<sup>1,2</sup> and Leif Ristroph<sup>1,†</sup>

<sup>1</sup>Applied Math Lab, Courant Institute, New York University, New York 10012, USA

<sup>2</sup>Center for Computational Biology, Flatiron Institute, Simons Foundation, New York 10010, USA



(Received 19 February 2018; published 31 August 2018)

We study how a suspended liquid film is deformed by an external flow en route to forming a bubble through experiments and a model. We identify a family of nonminimal but stable equilibrium shapes for flow speeds up to a critical value beyond which the film inflates unstably, and the model accounts for the observed nonlinear deformations and forces. A saddle-node or fold bifurcation in the solution diagram suggests that bubble formation at high speeds results from the loss of equilibrium and at low speeds from the loss of stability for overly inflated shapes.

DOI: 10.1103/PhysRevLett.121.094501

Soap films and bubbles are fascinating from many perspectives, not the least being the physics and mathematics of their shapes. Dipping a wire frame in soapy water yields a thin film that, due to surface tension, forms what can be idealized as a surface of minimal area [1–3]. Its shape is dictated by the Young-Laplace equation, which relates the pressure difference across an interface to its mean curvature [3,4]. The equality of pressures across an open film implies an equilibrium shape whose curvature is everywhere zero, and identifying such minimal surfaces consistent with a boundary has been a classic problem since first studied by Lagrange and Plateau [5–7]. Similarly, a spherical bubble is a closed surface that minimizes the area for a given volume. How a bubble is first formed involves the necking down and pinching off of a film. This event may be triggered, e.g., by separating two supports bridged by a liquid or film, as studied by Maxwell [8]. Recent work has focused on the collapse dynamics of fluid necks in the approach to pinch off [9–12] and on related topological transitions in films [13,14].

Our more common experience of making bubbles by blowing on a film is less studied and involves unique complexities. This event has been visualized in recent studies [15,16], and the competition of dynamic and Laplace pressures explains the critical flow speed needed to form bubbles [17]. Still unresolved is the flow-induced reshaping of a film, which even in equilibrium involves nonlinear deformations, incompressible flows into and around the film, and flow separation that forms a wake. These effects arise in other natural and industrial contexts, such as the ballooning and breakup of falling raindrops [18,19], water wave generation by wind [20], and the production of foams, emulsions, and sprays [21,22]. The mutual influence of interface shape and flow is a feature shared with many fluid-structure interactions [23,24], whose study often benefits from clean settings for a comparison of experiment and theory.

Here we consider the bubble-blowing problem in which a film suspended across a ring is deformed by the uniform flow of an exterior fluid. Recalling Plateau's use of immiscible liquid-liquid systems [5], we study oil films in flowing water, a system that offers advantages over soap film in air by mitigating the effect of gravity, eliminating evaporation, and permitting precise flow control, conditioning, and visualization. We also numerically construct 2D equilibria of a film distended by an inviscid but separated flow, with stable shapes qualitatively matching those seen in experiments and unstable shapes offering insight into how a bubble is blown.

*Experiments.*—We exploit a serendipitous discovery that some common oils can form large and long-lived films within water. By passing a wire loop through a layer of olive oil and into water below, one forms films that last for minutes before rupturing due to thinning by draining of the buoyant oil [25]. We employ olive oil as the interior fluid of density  $\rho_i = 0.91 \text{ g/cm}^3$  immersed in the exterior fluid of

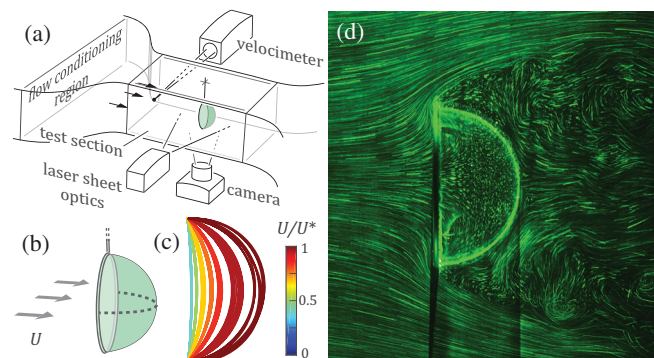


FIG. 1. Experiments. (a) Apparatus for studying the shape of, and flow around, an oil film in flowing water. (b) Schematic. (c) Measured profiles of stable shapes for speeds  $U$  up to  $U^*$ , at which the film ruptures. (d) Flow field near  $U/U^* = 1$  for a ring of radius  $R = 2 \text{ cm}$ .

water,  $\rho_e = 1.00 \text{ g/cm}^3$ ; their coefficient of surface tension is  $\gamma = 17 \pm 1 \text{ dyn/cm}$ , consistent with previous measurements [26]. The existence of stable films larger than the capillary length,  $\sqrt{\gamma/(\rho_e - \rho_i)g} = 0.4 \text{ cm}$ , suggests the presence of surfactants in the oil, perhaps residuals from processing [27]. To study the response to flow, we devise an apparatus that sits atop a water tunnel and allows for the repeatable formation of films on wire rings of radius  $R = 1\text{--}3 \text{ cm}$ . As shown in Figs. 1(a) and 1(b), the broadside of the ring faces the uniform oncoming flow of far-field speed  $U = 1\text{--}10 \text{ cm/s}$  that can be varied and measured. The external flow is dominated by inertia at these high Reynolds numbers:  $\text{Re} = \rho_e UR/\mu_e \sim 10^3$ , where  $\mu_e = 1 \text{ cP}$  is the viscosity of water. The flow-film interaction involves hydrodynamic and surface tension pressures, whose ratio is the Weber number  $\text{We} \propto \rho_e U^2 R/\gamma \sim 1$ , a scaled version of which will serve as the control parameter for this study.

When a film is placed within a flow of moderate speed, it is deformed from planar and settles to a dome- or parachutelike shape. The film then seems to be in stable equilibrium: It persists for minutes and recovers its shape after impulsive perturbations to the support or the flow speed. Such shapes exist up to a critical flow speed  $U^*$ , beyond which the film inflates unstably and ruptures (see Supplemental movie [28]). In Fig. 1(c), we show measured profiles for a ring of radius  $R = 2.0 \text{ cm}$  for several values of  $U$  up to  $U^* = 6.9 \text{ cm/s}$ ; 15 trials are shown at each of seven speeds selected from a set of 16 speeds. The film is nearly planar at low speeds and deforms into a hollow hemispherelike cavity as  $U \rightarrow U^*$ . However, the response is nonlinear in  $U$ , with the strongest changes occurring in the immediate lead-up to rupture. Additional analysis of the profile shapes is presented as Supplemental Material [28].

A visualization study reveals the character of the external flow. The photograph in Fig. 1(d) shows flow path lines [29] as revealed by microparticles illuminated by a planar laser sheet shone near the equator of a highly deformed film. Visual tracing of the incoming flow shows that only fluid very near the midline enters the cavity, where it abruptly slows down, as indicated by the short path lines. This internal flow slowly reverses course, following the inner contour of the film before abruptly speeding up and exiting near the support, where it separates from the surface to leave a large wake downstream.

*Model.*—To gain insight into the general features seen in experiments, we formulate a film-flow interaction model in a 2D setting, for which separated-flow models are well developed [30]. Flow separation is indeed a key ingredient, as purely inviscid and attached flow generates no pressure difference (akin to d’Alembert’s paradox [29]) and, thus, no film deformation. We consider a 2D exterior flow that is inviscid, incompressible, and irrotational and, hence, may be represented by a velocity potential in the complex plane. Separation is accounted for by Levi-Civita’s free-streamline

theory formulation [24,30,31], which uses conformal mapping [32] to solve for the potential as well as the path of the free or separation streamlines that shed tangentially from the pinning points and enclose a wake. Following previous studies [23,24,33,34], the wake flow is not explicitly modeled, but rather the wake pressure is assumed uniform, consistent with experimental measurements of the back pressure on bodies at high  $\text{Re}$  [35]. The film is viewed as a 1D curve pinned to two points separated by a (vertical) distance  $2R$  and immersed within the exterior fluid of density  $\rho_e = \rho$ . The tension coefficient is  $\gamma$ , and the far-field flow is horizontal with speed  $U$ . The film is assumed static, and its equilibrium shape arises from the Young-Laplace law, which prescribes a local balance of differential hydrodynamic pressure and the surface tension pressure associated with curvature.

We highlight key steps of the model formulation, and supporting details are given in Supplemental Material [28]. Up-down symmetry permits focus on the half-space problem, and the film profile is given by the tangent angle  $\theta(\sigma)$ , where the parameter  $\sigma \in [0, \pi/2]$  traverses the film. The local flow velocity  $\mathbf{u}$  along the film has a direction given by  $\theta$  to ensure no penetration, and previous work [24] shows that the tangential speed  $|\mathbf{u}|$  satisfies

$$|\mathbf{u}| = e^{\tau(\sigma)}, \quad \text{where } \tau = \mathcal{H}[\theta] \quad (1)$$

and  $\mathcal{H}$  is the Hilbert transform. Crucially, this indicates that the flow speed along the film can be computed from the shape alone. A second flow-shape relationship is furnished by combining the Young-Laplace and Bernoulli laws. The former relates the local pressure difference across an interface to its mean curvature, which for a zero-pressure wake and a film (two interfaces) yields  $\Delta p = p = 2\gamma\kappa$ . The latter relates the pressure and speed in the exterior flow:  $p + \frac{1}{2}\rho|\mathbf{u}|^2 = \frac{1}{2}\rho U^2$ . Combining to eliminate  $p$  yields the dimensionless curvature

$$\kappa R = R d\theta/ds = \eta[1 - (|\mathbf{u}|/U)^2], \quad \eta = \rho U^2 R/4\gamma, \quad (2)$$

where  $s$  is the arc length and  $\eta$  is akin to the Weber number. Recasting the above relationship in integral form yields

$$\theta(\sigma) = -\frac{\pi}{2} + K\eta \int_{\sigma}^{\pi/2} \sinh[\tau(\sigma')] \sin 2\sigma' d\sigma', \quad (3)$$

where the constant  $K$  is determined by the pinning condition at  $\sigma = 0$ . Solving this equation numerically by a Broyden method yields the equilibrium shape  $\theta(\sigma)$  as a function of the dimensionless parameter  $\eta$ . The hydrodynamic force on the film is then given by an integral of pressure, and the entire 2D velocity and pressure fields can also be reconstructed.

We find that solutions exist only for  $\eta \leq \eta^* \approx 1.0015$ , which we associate with rupture. Selected profile shapes are shown in Fig. 2(a) at equally spaced  $\eta/\eta^* \in [0, 1]$ . In

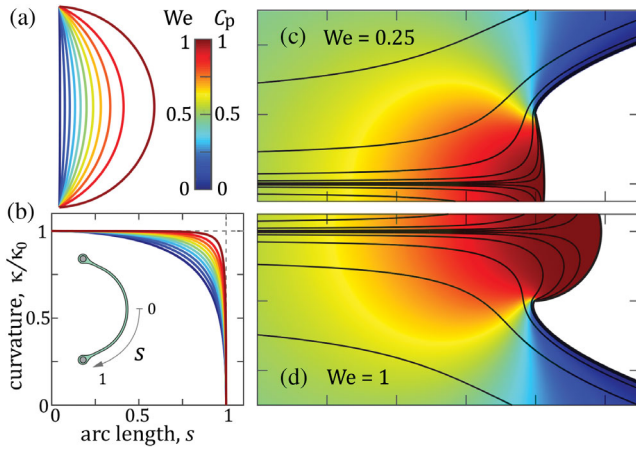


FIG. 2. Free-streamline theory model. (a) Equilibrium solutions at equally spaced  $\eta = \rho U^2 R / 4\gamma$ . (b) Profile curvature for the same solutions. (c),(d) Streamlines (black curves) and pressure coefficient  $C_p$  (color map) for  $\eta/\eta^* = 0.25$  and 1. The wake (white) and far field have  $C_p = 0$ .

Fig. 2(b), we show the profile curvature  $\kappa$  scaled by its maximal value  $\kappa_0 = \kappa(s=0) = \eta/R$  at the stagnation point and plotted versus the scaled arc length, where  $s=0, 1$  denote the stagnation and separation points, respectively (see the inset). For each forcing, the curvature drops from its peak at stagnation to a value of zero at separation. For low  $\eta/\eta^*$  this drop is gradual, but as  $\eta/\eta^* \rightarrow 1$  an ever greater portion of the interface takes on a value near  $\kappa_0$ , and the shapes thus more closely resemble circular arcs.

In Figs. 2(c) and 2(d), selected streamlines (black curves) and the dimensionless pressure coefficient  $C_p = 2p/\rho U^2 = 1 - (|u|/U)^2$  (color map) are compared for weak and strong forcing. The presence of the interface slows the oncoming flow, leading to higher pressures (red) in front, but the strongly deformed film of  $\eta/\eta^* = 1$  has

particularly large stagnated region inside the cavity where the pressure is more uniformly high. The streamlines show that a thin filament of incoming fluid spreads upon entering the cavity, dropping in speed (as required by continuity or mass conservation) and thus increasing in pressure (by Bernoulli's law). In essence, the stagnation point has spread into a broad region that encompasses much of the interface. These results indicate that the approach to rupture is marked by a tendency towards uniform pressure difference across the interface and, by the Young-Laplace law, uniform curvature.

*Shape and force response.*—The 3D film in the experiments differs from the 2D model in that both principal curvatures of the Young-Laplace law are nonzero:  $\Delta p = 2\gamma(\kappa_1 + \kappa_2)$ . Assuming axisymmetry, this leads to  $\kappa_1 = \kappa_2 = \eta/2R$  at stagnation and  $\kappa_1 = -\kappa_2$  at separation, and generally one expects different shape solutions in 3D and 2D [28]. A comparison of the model and experiment, however, reveals some common trends. The model indicates that 2D film rupture is associated with a critical  $\eta^*$  very near unity, and experiments on several ring sizes reveal a somewhat higher  $\eta^* = \rho U^{*2} R / 4\gamma = 1.41 \pm 0.03$ . In Fig. 3, we characterize the shape response to increasing  $\eta$ , normalized by the appropriate  $\eta^*$  for 2D and 3D. The plot in Fig. 3(a) shows the maximal deformation as measured (colored points) and computed (black curve), with both showing that the response is nonlinear even in  $\eta \sim U^2$ . A second parameter pertains to the extension of the film, as quantified by the surface area  $S$  in 3D and the total arc length  $L$  in 2D [Fig. 3(b)]. These quantities, when multiplied by  $\gamma$ , determine the surface energies stored in 3D and 2D interfaces, respectively [3,4]. The transition from flat (disk or line segment) at  $\eta/\eta^* = 0$  to a hollow (hemispherical or semicircular) cavity at  $\eta/\eta^* = 1$  yields the expected limits of  $S/R^2 = \pi, 2\pi$  and  $L/R = 2, \pi$ . The response is again nonlinear, with most extension occurring in the immediate approach to  $\eta/\eta^* = 1$ .

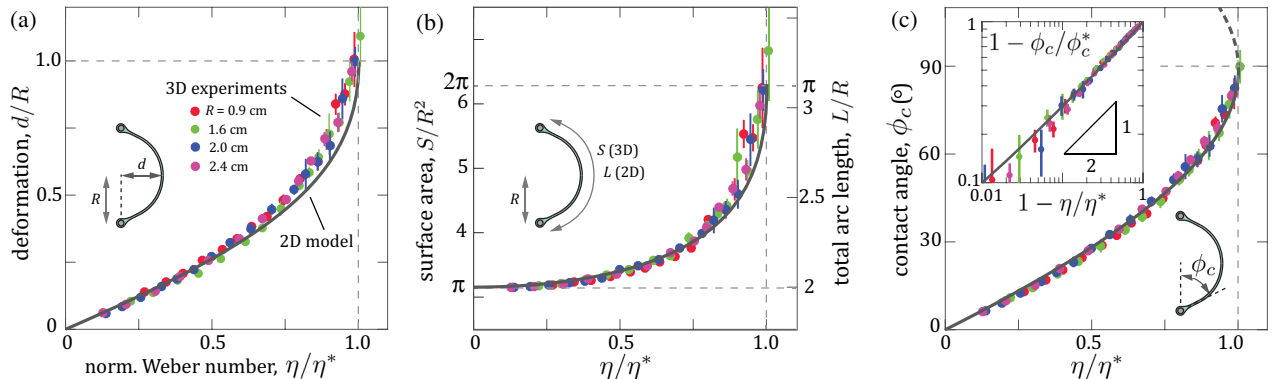


FIG. 3. Shape characterization. (a) Maximal deformation of the film versus normalized Weber number  $\eta/\eta^*$  in experiments (colored dots) and the model (black curve). (b) Film surface area  $S$  (experiments, left axis) and arc length  $L$  (model, right axis). (c) Contact angle  $\phi_c$  of a film with support, with stable (solid curve) and unstable (dashed curve) branches from the model. The inset plot reveals a  $1/2$  power typical of a fold bifurcation, with  $\phi_c^*$  being the critical contact angle at rupture. Error bars for each experimental point represent standard deviations over 15 trials.

The contact angle  $\phi_c$  of the film with the support, as defined in Fig. 3(c), also steeply increases en route to rupture at  $\eta/\eta^* = 1$  and approaches  $\phi_c^* \approx 90^\circ$  in experiments. The model reveals a second branch of solutions that can be accessed by decreasing  $\eta/\eta^*$  near this point. These interfaces have  $\phi_c > 90^\circ$  and are overinflated into super-semicircular arcs. Superhemispherical shapes are never observed in experiments, suggesting that this upper branch represents unstable equilibria. This solution structure also indicates that overinflation is associated with a critical point in a saddle-node or fold bifurcation that occurs in the parameter  $\eta/\eta^*$ . To quantify this behavior, we consider a log-scaled plot of  $1 - \phi_c/\phi_c^*$  versus  $1 - \eta/\eta^*$  [Fig. 3(c), inset], which reveals a power-law approach to the critical point, here  $(1 - \eta/\eta^*) \rightarrow 0$ . The observed power near  $1/2$  for both experiments and the model is typical of a saddle-node bifurcation [36]. Further analysis of the solutions can be found in Supplemental Material [28], including an argument supporting the stability of the lower branch and instability of the upper.

The contact angle also relates to the total hydrodynamic force exerted on the film. Integration of the pressure, which is proportional locally to the curvature, yields a formula for the force on a 3D axisymmetric film [28]:  $F = 4\pi R\gamma \sin \phi_c$ . The 2D analogue is a force per unit length of  $F = 4\gamma \sin \phi_c$ . Each case reveals a maximal force  $F^*$  (of  $4\pi R\gamma$  in 3D and  $4\gamma$  in 2D) that can be supported, which occurs for  $\phi_c^* = 90^\circ$ . From this perspective, overinflation occurs because the surface tension is unable to resist the imposed forces. The formula also provides a means for inferring the total force (here a drag) from the experimentally measured contact angle, and these data are shown as colored points in Fig. 4(a). The force extracted from the model (black curve) shows a similar trend, with no significant change in behavior as  $\eta/\eta^* \rightarrow 1$ , unlike the shape parameters in Fig. 3.

Close inspection of the force data reveals subtle nonlinearities, which correspond to deviations from the  $U^2$  scaling expected for bodies of fixed shape in fast flows [29]. Indeed, the effect of shape is highlighted by the force coefficient  $C_F = 2F/\rho_e U^2 A$ , where  $A = \pi R^2$  is the frontal area presented to the flow, which removes the expected scaling with the speed and size. This 3D coefficient and its 2D analogue of  $F/\rho U^2 R$  for the model are shown in Fig. 4(b). Both increase with  $\eta/\eta^*$ , indicating an “anti-streamlining” behavior in which drag grows more strongly than  $U^2$  as increasingly draggy parachutelike shapes are generated. The extremes of  $\eta/\eta^* = 0, 1$  also correspond well with known values of  $C_F \approx 1.2$  for a planar disk [37] (0.88 for a plate in the free-streamline theory [30]) and 1.4–1.5 for a hollow hemisphere [38]. A signature of the higher drag for greater  $\eta/\eta^*$  may also be seen in the wider wake in Fig. 2(d) as compared to Fig. 2(c).

The shape and force characterizations can be combined by assessing the force-displacement or stress-strain relationship, plotted as the dimensionless force  $F/F^*$  versus deformation  $d/R$  in Fig. 4(c). The film is Hookean for small forces, but thereafter the strain softens, yielding ever more in response to incrementally increased forcing.

*Discussion.*—This work reveals equilibrium shapes of flow-forced interfaces, which, unlike the area-minimizing surfaces formed by films and bubbles under hydrostatic conditions, have nonzero and nonuniform curvature. A model that solves for such shapes in 2D by locally balancing the Laplace and hydrodynamic pressures on a film in an inviscid but separated flow reproduces qualitative features and trends seen in 3D-axisymmetric experiments, including a nonlinear shape response leading up to rupture. The model also reveals a branch of unstable equilibria connected to the stable branch at the critical point of a fold bifurcation. This solution structure suggests that an unbounded distension of the film occurs at high speeds

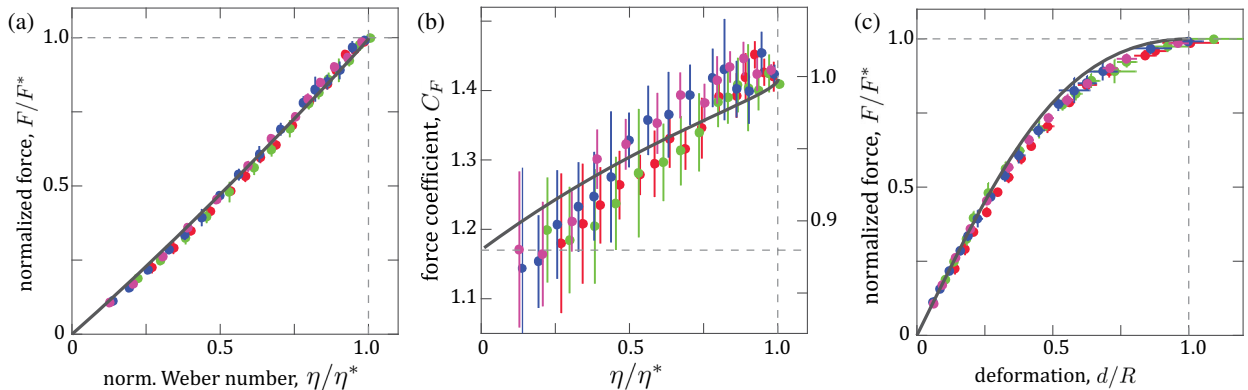


FIG. 4. Force characterization in experiments (dots) and the model (curve). (a) Total hydrodynamic force normalized by maximal values of  $F^* = 4\pi R\gamma$ ,  $4\gamma$  for 3D and 2D, respectively. (b) Force coefficients for 3D experiments (left axis) and the 2D model (right axis). The horizontal dashed line indicates drag coefficient values determined experimentally for a disk [37] and theoretically for a plate [30]. (c) A force-displacement plot shows strain softening in the approach to rupture. Experimental errors in  $F/F^* = \sin \phi_c$  and  $C_F = 2 \sin \phi_c / \eta$  are propagated from measured variations in  $\phi_c$ .

beyond the critical point where no equilibria exist and also at lower speeds for which overly inflated shapes are unstable. These insights could be put to use in flow metrology, such as in designing film-based pressure probes or tensiometers, and in fluidic applications related to droplets, vesicles, and emulsions [39,40].

For our everyday experience with soap films, these findings offer a quasistatic picture of how an initially flat film is deformed by blowing at increasing speed before overinflating and forming a bubble. Surface tension opposes the imposed aerodynamic pressure across the film, which increasingly softens until the resisting force reaches its upper limit and the material fails. For the constant and uniform flow studied here, this failure involves overinflation, thinning, and rupture rather than making a water-filled oil bubble. In contrast, the birth of a soap bubble in air may result from the cessation of blowing once the film is overinflated. Indeed, an oil bubble can be generated underwater by an impulsive motion of the ring [28]. The form of the oncoming flow (i.e., uniform versus jetlike [17]) and the densities of two fluids (which impact the pinching dynamics) are additional factors that may decide between the ultimate fates of a ruptured film versus a blown bubble.

We thank S. Childress and J. Zhang for useful discussions. We acknowledge support from the grant NSF-CBET-1805506, from the postdoctoral fellowship NSF-DMS-1400934 to A. U. O., and from the Lilian and George Lyttle Chair.

---

\*Present address: Department of Mathematical Sciences, New Jersey Institute of Technology, New Jersey, USA.

†ristroph@cims.nyu.edu

- [1] C. V. Boys, *Soap Bubbles, Their Colors and the Forces which Mold Them* (Dover, New York, 1959).
- [2] F. J. Almgren and J. E. Taylor, *Sci. Am.* **235**, 82 (1976).
- [3] C. Isenberg, *The Science of Soap Films and Soap Bubbles* (Dover, New York, 1992).
- [4] P.-G. De Gennes, F. Brochard-Wyart, and D. Quéré, *Capillarity and Wetting Phenomena: Drops, Bubbles, Pearls, Waves* (Springer, New York, 2013).
- [5] J. Plateau, *Mém. Acad. R. Sci., Lett. Beaux-Arts Belg.* **23**, 1 (1849).
- [6] J.-L. Lagrange, *Oeuvres de Lagrange* (Gauthier-Villars, Paris, 1870), Vol. 1.
- [7] R. Courant, *Am. Math. Mon.* **47**, 167 (1940).
- [8] J. C. Maxwell, in *The Scientific Letters and Papers of James Clerk Maxwell* (Cambridge University Press, Cambridge, England, 1990).
- [9] I. Cohen, M. P. Brenner, J. Eggers, and S. R. Nagel, *Phys. Rev. Lett.* **83**, 1147 (1999).
- [10] J. Eggers and E. Villermaux, *Rep. Prog. Phys.* **71**, 036601 (2008).
- [11] W. van Hoeve, S. Gekle, J. H. Snoeijer, M. Versluis, M. P. Brenner, and D. Lohse, *Phys. Fluids* **22**, 122003 (2010).
- [12] J. Bostwick and P. Steen, *Annu. Rev. Fluid Mech.* **47**, 539 (2015).
- [13] R. E. Goldstein, J. McTavish, H. K. Moffatt, and A. I. Pesci, *Proc. Natl. Acad. Sci. U.S.A.* **111**, 8339 (2014).
- [14] H. K. Moffatt, R. E. Goldstein, and A. I. Pesci, *Phys. Rev. Fluids* **1**, 060503 (2016).
- [15] D. Kim, S. J. Yi, H. D. Kim, and K. C. Kim, *J. Visualization* **17**, 337 (2014).
- [16] J. Davidson and S. Ryu, *J. Visualization* **20**, 53 (2017).
- [17] L. Salkin, A. Schmit, P. Panizza, and L. Courbin, *Phys. Rev. Lett.* **116**, 077801 (2016).
- [18] J. E. McDonald, *J. Meteorol.* **11**, 478 (1954).
- [19] A. Wierzbna, *Exp. Fluids* **9**, 59 (1990).
- [20] O. M. Phillips, *J. Fluid Mech.* **2**, 417 (1957).
- [21] D. L. Weaire and S. Hutzler, *The Physics of Foams* (Clarendon, Oxford, 1999).
- [22] P. Marmottant and E. Villermaux, *J. Fluid Mech.* **498**, 73 (2004).
- [23] S. Alben, M. Shelley, and J. Zhang, *Nature (London)* **420**, 479 (2002).
- [24] S. Alben, M. Shelley, and J. Zhang, *Phys. Fluids* **16**, 1694 (2004).
- [25] K. J. Mysels, *Soap Films: Studies of Their Thinning and a Bibliography* (Pergamon, New York, 1959).
- [26] P. Than, L. Preziosi, D. D. Joseph, and M. Arney, *J. Colloid Interface Sci.* **124**, 552 (1988).
- [27] D. Boskou, *Olive Oil: Chemistry and Technology* (American Oil Chemists' Society, Urbana, IL, 2015).
- [28] See Supplemental Material at <http://link.aps.org/supplemental/10.1103/PhysRevLett.121.094501> for text and two videos.
- [29] D. J. Tritton, *Physical Fluid Dynamics* (Clarendon, Oxford, 1988).
- [30] L. M. Milne-Thomson, *Theoretical Hydrodynamics* (Dover, New York, 1968).
- [31] A. R. Elcrat and L. N. Trefethen, *J. Comput. Appl. Math.* **14**, 251 (1986).
- [32] J. W. Brown and R. V. Churchill, *Complex Variables and Applications* (McGraw-Hill, New York, 2009).
- [33] L. Ristroph, M. N. Moore, S. Childress, M. J. Shelley, and J. Zhang, *Proc. Natl. Acad. Sci. USA* **109**, 19606 (2012).
- [34] M. N. Moore, L. Ristroph, S. Childress, J. Zhang, and M. J. Shelley, *Phys. Fluids* **25**, 116602 (2013).
- [35] R. Fail, R. Eyre, and J. Lawford, Aeronautical Research Council, Technical Report No. 3120, 1959.
- [36] S. H. Strogatz, *Nonlinear Dynamics and Chaos* (Westview, Boulder, CO, 2014).
- [37] F. W. Roos and W. W. Willmarth, *AIAA J.* **9**, 285 (1971).
- [38] H. G. Heinrich and E. L. Haak, Aeronautical Systems Division, Technical Report No. 61-587, 1961.
- [39] A. Utada, E. Lorenceau, D. Link, P. Kaplan, H. Stone, and D. Weitz, *Science* **308**, 537 (2005).
- [40] K. Funakoshi, H. Suzuki, and S. Takeuchi, *J. Am. Chem. Soc.* **129**, 12608 (2007).